



The Superior Properties of $\text{La}_{0.6}\text{Ba}_{0.4}\text{CoO}_{3-\delta}$ Thin Film Electrodes for Oxygen Exchange in Comparison to $\text{La}_{0.6}\text{Sr}_{0.4}\text{CoO}_{3-\delta}$

Ghislain M. Rupp,² Alexander Schmid, Andreas Nennung, and Jürgen Fleig*

Institute of Chemical Technologies and Analytics, Vienna University of Technology, Vienna, A-1060, Austria

The electrochemical properties of $\text{La}_{0.6}\text{Ba}_{0.4}\text{CoO}_{3-\delta}$ (LBC) and $\text{La}_{0.6}\text{Sr}_{0.4}\text{CoO}_{3-\delta}$ (LSC) dense thin film model electrodes, deposited by pulsed laser deposition at 600°C on yttria-stabilized zirconia (100) electrolytes, were investigated by electrochemical impedance spectroscopy (EIS) at 450–600°C and 10^{-4} to 1 bar $p\text{O}_2$. This comparative study reveals the influence of the A-site dopant size on the catalytic activity for the oxygen exchange, chemical capacitance and electronic conductivity. For both thin films the overall oxygen reduction is still limited by the oxygen surface exchange, although an extraordinarily high activity for the oxygen reduction reaction (ORR) was measured (LBC $\sim 0.18 \text{ } \Omega\text{cm}^2/\text{LSC} \sim 0.6 \text{ } \Omega\text{cm}^2$ at 604°C and 0.21 bar $p\text{O}_2$). Moreover, LBC exhibits a rather low activation energy for the ORR ($1.19 \pm 0.11 \text{ eV}$) together with a high electronic conductivity ($839 \text{ S} \cdot \text{cm}^{-1}$ at $\sim 442^\circ\text{C}$). Based on these excellent electrochemical properties, LBC may also be a highly promising material for porous cathodes in intermediate temperature (400–600°C) solid oxide fuel cells.

© The Author(s) 2016. Published by ECS. This is an open access article distributed under the terms of the Creative Commons Attribution 4.0 License (CC BY, <http://creativecommons.org/licenses/by/4.0/>), which permits unrestricted reuse of the work in any medium, provided the original work is properly cited. [DOI: 10.1149/2.1061606jes] All rights reserved.

Manuscript submitted January 22, 2016; revised manuscript received March 11, 2016. Published March 26, 2016.

Solid oxide fuel cells (SOFCs) are very promising devices for efficient energy conversion to meet the world's continuously increasing demand of energy. The advantage of fuel flexibility ranging from pure hydrogen to a variety of hydrocarbon fuels and natural gas is one of the most attractive features.^{1–3} Despite all its benefits, SOFC technology is also demanding and a lot of efforts have been made over the past decades to optimize important key factors for commercialization such as durability, manufacturing cost and modularization.^{4–7} The simplest approach to increase long term stability of SOFC systems is to lower the operating temperatures in order to avoid unfavorable side reactions of different components.⁸ However, a temperature decrease also lowers the kinetics of processes exhibiting high activation energies, especially the oxygen reduction reaction (ORR). Special attention is therefore put on the search and improvement of cathode materials since the ORR is considered to currently limit the performance of intermediate temperature SOFCs.^{9,10}

Oxides were introduced as cathode materials to substitute expensive noble metals and one prominent example already employed in commercially available SOFCs is $\text{La}_x\text{Sr}_{1-x}\text{MnO}_{3-\delta}$ (LSM). It offers a high electronic conductivity, acceptable catalytic activity for the oxygen exchange and sufficient chemical stability, but due to its low ionic conductivity it is unattractive for SOFCs operating at intermediate temperatures (400–600°C). Mixed ionic and electronic conductors (MIECs) of the perovskite-type solid-solution $\text{La}_{1-x}\text{Sr}_x\text{Co}_{1-y}\text{Fe}_y\text{O}_{3-\delta}$, can extend the reaction zone from the triple phase boundary (electrode-electrolyte-gas) to the two phase boundary due to their excellent ionic conductivity. They also offer high catalytic activity for the oxygen exchange and thus have been in the focus of recent research.^{11,12} For a given Sr concentration, e.g. $x = 0.4$, the catalytic activity, oxygen vacancy concentration and thus the ionic conductivity increase with the amount of Co on the B-site of the perovskite, though, at the expense of a reduced chemical stability.¹³ Furthermore, changes of the electronic structure are observed from semiconductor-like for $\text{La}_{0.6}\text{Sr}_{0.4}\text{FeO}_{3-\delta}$ (LSF64) to metal-like behavior for $\text{La}_{0.6}\text{Sr}_{0.4}\text{CoO}_{3-\delta}$ (LSC64) at SOFC operating conditions.¹⁴ The detailed influence of the B-site metal cation and of the Sr dopant concentration on the electrochemical properties were key aspects of numerous studies,^{15–20} while much less investigations dealt with the effect of alternative A-site dopants.¹⁶

In this study, the electrochemical properties of well-defined LSC64 and $\text{La}_{0.6}\text{Ba}_{0.4}\text{CoO}_{3-\delta}$ (LBC64) are directly compared with each other. The advantage of comparing these two identically charged dopants is that almost all the chemical and electrochemical differences originate from the different ionic radii of Sr^{2+} (144 pm) and Ba^{2+} (161

pm),²¹ since both atomic Sr and Ba have a similar valence electron configuration ($5s^2$; $6s^2$). Nonetheless, the defect structure and thus the MIEC properties differ significantly due to a higher reducibility of the perovskite-type lattice with Ba ions.^{22,23} To the best of the authors' knowledge, electrochemical investigations of $\text{La}_{1-x}\text{Ba}_x\text{CoO}_{3-\delta}$ (LBC) electrodes have been only performed on porous systems^{24–28} including mixtures of LBC with GDC.²⁹ These studies already reported comparatively low polarization resistances, but were not able to deconvolute the surface exchange and transport resistances of LBC for geometrical reasons. Therefore, dense thin film model electrodes were used in this work and the catalytic activity for the oxygen exchange could be determined for LSC and LBC over an oxygen partial pressure range of 10^{-4} to 1 bar $p\text{O}_2$ and at temperatures between 450 and 600°C. The results reveal the superior properties of LBC in terms of catalytic activity for oxygen exchange, in comparison to most state of the art MIECs for intermediate SOFCs.

Experimental

Thin film preparation.—Targets for deposition of LSC thin films by pulsed laser deposition (PLD) were synthesized from powders prepared by Pechini synthesis.³⁰ La_2O_3 , SrCO_3 , BaCO_3 and Co powders (all Sigma Aldrich, 99.995%) were individually dissolved in nitric acid, mixed in appropriate ratios and citric acid (TraceSELECT, 99.9998%) was added for chelation. A calcination step was performed at 1000°C, followed by isostatical pressing ($\sim 150 \text{ MPa}$) of the powder to a pellet and a sintering procedure at 1200°C for 12 hours in air, thus yielding a $\text{La}_{0.6}\text{Sr}_{0.4}\text{CoO}_{3-\delta}$ and a $\text{La}_{0.6}\text{Ba}_{0.4}\text{CoO}_{3-\delta}$ target for PLD.

The LSC and LBC thin films were deposited onto (100) oriented yttria stabilized zirconia (YSZ, 9.5 mol% Y_2O_3 , Crystec GmbH, Germany) single crystals with a thickness of 0.5 mm and a size of $5 \times 5 \text{ mm}^2$ or $10 \times 10 \text{ mm}^2$. Epipolished substrates were used to prepare symmetrical samples with nominally identical thin films on both sides of the YSZ for impedance measurements. Ablation of the target material was carried out by a KrF ($\lambda = 248 \text{ nm}$) excimer laser (Lambda COMPexPro 201F) operated at a pulse repetition rate of 5 Hz, a pulse duration of 50 ns and a laser fluence of approximately $1.5 \text{ J} \cdot \text{cm}^{-2}$ at the target. The atmosphere was set to $4 \cdot 10^{-2}$ mbar oxygen partial pressure and the substrate was heated to a surface temperature of 600°C. By applying 9,150 laser pulses to the LSC and 8,175 laser pulses to the LBC target, thin films of approx. 300 nm thickness were grown on the substrate (substrate to target distance = 6 cm). After deposition, the sample was cooled in the deposition atmosphere at a cooling rate of $12^\circ\text{C} \cdot \text{min}^{-1}$. The substrate was flipped and the PLD procedure was again repeated for the back side. Prior to the impedance measurements, the $5 \times 5 \text{ mm}^2$ samples were broken into pieces of about $1.5 \times 1.5 \text{ mm}^2$ to minimize the influence of electronic sheet

*Electrochemical Society Member.

²E-mail: ghislain.rupp@tuwien.ac.at

resistance, see also EIS – Initial measurements and equivalent circuit model section. It is noteworthy that the sample surface was never exposed to “cleaning” treatments after deposition in order to avoid any reactions and contamination from solvents including H_2O .³¹

Structural characterization.—The PLD target material was analyzed in Bragg Brentano geometry by a X’Pert Powder (PANalytical) diffractometer. A thin film diffraction pattern was obtained using a D8-Discover instrument (Bruker AXS) in parallel beam geometry equipped with a general area detector diffraction system (GADDS). Secondary electron microscopy was performed on a FEI Quanta 200 field emission gun scanning electron microscope equipped with an Everhart-Thornley detector.

Electrochemical measurements.—All annealing and impedance experiments were performed in a cleaned quartz tube which was evacuated and refilled several times with the desired high purity N_2 (ALPHAGAZ 1 >99.999 mol% nitrogen)/ O_2 (ALPHAGAZ 1 >99.998 mol% oxygen) mixture before the sample was uniformly heated in a tube furnace. The symmetrical samples (thin film – YSZ – thin film) were sandwiched between two platinum foils for impedance measurements. The electronic connection in the sample holder consisted of Pt wires and a non-encapsulated type S thermoelement was used for temperature measurement. No materials other than Pt, quartz and the sample itself were heated during impedance measurement and annealing. All these precautions were taken in order to obtain electrochemical measurements that do not suffer from any cathode poisoning. It took approximately 45 minutes to heat the sample to the desired temperature (thermal equilibration), then the different impedance measurement series were performed. The impedance was measured by a Novocontrol Alpha A High Performance Frequency Analyzer in the frequency range from 10^6 to a minimum of $5 \cdot 10^{-3}$ Hz with a resolution of five points per decade and an alternating voltage of 10 mV (rms) applied between the two thin film electrodes.

In-plane resistivity measurements of the thin films were also performed in a quartz tube. Four platinum needles were placed on top of the thin film in the corners of a $10 \times 10 \text{ mm}^2$ sample as close as possible to the sample boundary to meet the prerequisites of the van der Pauw method.³² The quartz apparatus was uniformly heated in a tube furnace and temperature was measured by means of an encapsulated type K thermoelement positioned adjacent to the sample. A mixture of high purity N_2/O_2 was used to realize an oxygen partial pressure of 0.21 bar. A precision voltage source (Keithley 2410) and a multimeter (Keithley 2000) were used during the course of the measurements.

Results

Structural characterization.—The thin film morphology of both freshly deposited perovskite layers on top of the YSZ electrolyte was investigated by FESEM. Top views and cross-sections of the samples are shown in Fig. 1. Cross-sections of the thin films were achieved by fracturing of the samples. The electronically conducting thin films are clearly distinguishable from the blurry image of the non-conductive substrate. Therefore, the film thicknesses (LSC $\approx 420 \text{ nm}$; LBC $\approx 410 \text{ nm}$ in Fig. 1) could be estimated from SEM-images and deposition parameters were then adjusted to obtain $300 \pm 10 \text{ nm}$ thin films for both materials. Both thin films show a very similar dense packing of columnar shaped grains, which is expected for the PLD growth conditions applied.^{33,34} No voids or pinholes were observed in the cross-sections. For both materials crack formation could not be avoided, as seen in the top views in Fig. 1. Crack formation most probably takes place after completing thin film deposition during cooling and is driven by the difference of thermal expansion coefficients between thin films (LSC64³⁵ = $20.5 \cdot 10^{-6} \text{ K}^{-1}$, LBC64²⁷ = $22.3 \cdot 10^{-6} \text{ K}^{-1}$) and substrate (YSZ³⁶ = $10.8 \cdot 10^{-6} \text{ K}^{-1}$). From previous measurements on similar LSC64 thin films an enhanced true surface area due to crack formation of up to 30% was estimated.³¹ However, quantities extracted by EIS in this study were still normalized to the projected electrode surface area. Most cracks can be assumed to not penetrate the entire

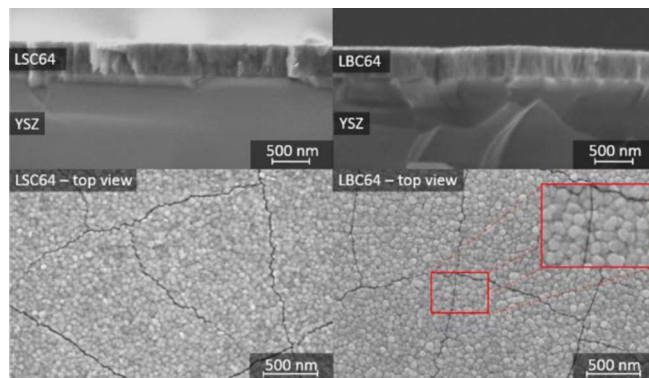


Figure 1. SEM images of LSC (l.h.s.) and LBC (r.h.s.) thin films. Cross sections are shown on the top and the surface on the bottom.

film, otherwise in-plane conductivities (see Van der Pauw – electronic conductivity section) should be much smaller.

PLD target and thin film structure were examined in Bragg-Brentano 2Θ - Θ geometry with focusing and parallel-beam optics, respectively. LSC64 and LBC64 target as well as thin film diffraction patterns over the measured 2Θ range are shown in Fig. 2. For both polycrystalline target diffraction patterns all visible peaks could be assigned to the perovskite phases and no sign of impurities was found. Vacancy ordering in LBC (annealed at high temperatures in Ar atmosphere) has been reported³⁷ for a similar cation stoichiometry ($\text{LaBaCo}_2\text{O}_{6.8}$). However, this tetragonal phase was not observed due to the oxidizing conditions applied during target preparation. The peaks of the diffraction patterns were indexed with respect to the pseudo-cubic structure of both materials since the rather small rhombohedral distortion of the crystal lattices could not be measured with the given resolution. For LSC64 and LBC64 rhombohedral angles α_r of 60.36° and 60.05° under standard conditions (298.15 K, 1 atm) can be calculated from literature.^{27,38} Both values are close to 60° – the value for a cubic crystal structure. Generally, changes in the crystal structure symmetry of the ABO_3 perovskite family can be explained by Goldschmidt’s tolerance factor t_f .³⁹ For LBC64 ($t_f \sim 1.00$) an almost ideal cubic structure is found in contrast to the more rhombohedrally distorted LSC64 ($t_f \sim 0.98$), calculated with ionic radii from.²¹ The pseudo cubic lattice parameter derived from the polycrystalline target diffraction patterns for LSC ($a_{pc} = 3.838 \pm 0.003 \text{ \AA}$) and LBC ($a_{pc} = 3.889 \pm 0.002 \text{ \AA}$) agree well with literature values.^{27,38}

The thin film patterns show the actual thin film growth relative to the (100) YSZ-plane. Therefore, both patterns are dominated by the intense (00l) peaks of the substrate. Again, no other peaks besides the substrate or the thin film peaks are found, indicating a sufficiently phase-pure deposition. Furthermore, it can be seen that both films grow preferentially in (100) and (110) direction on the substrate. Due to the

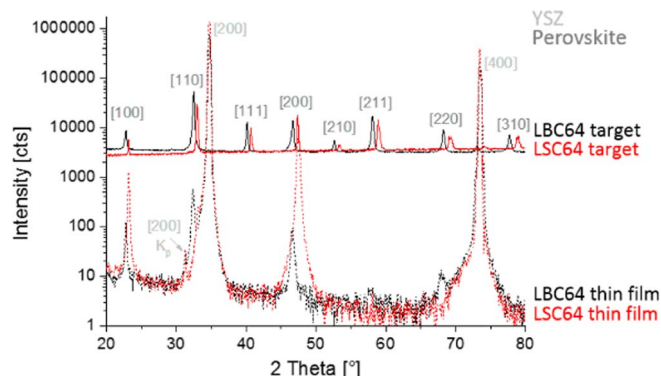


Figure 2. XRD pattern of LSC64 and LBC64 PLD target and thin film deposited on YSZ.

small amount of thin film peaks, the out-of-plane lattice parameters for LSC ($a_{pc} = 3.83 \pm 0.01 \text{ \AA}$) and LBC ($a_{pc} = 3.90 \pm 0.01 \text{ \AA}$) can be only given with limited accuracy.

EIS – Initial measurements and equivalent circuit model.—First, electrochemical impedance spectroscopy was used to measure the response of freshly deposited LSC and LBC thin films at $604 \pm 2^\circ\text{C}$ in synthetic air and 0.21 bar oxygen partial pressure ($p\text{O}_2$). Nyquist plots normalized to the projected electrode surface area are shown in Fig. 3a for LSC and Fig. 3b for LBC, a comparison between the two

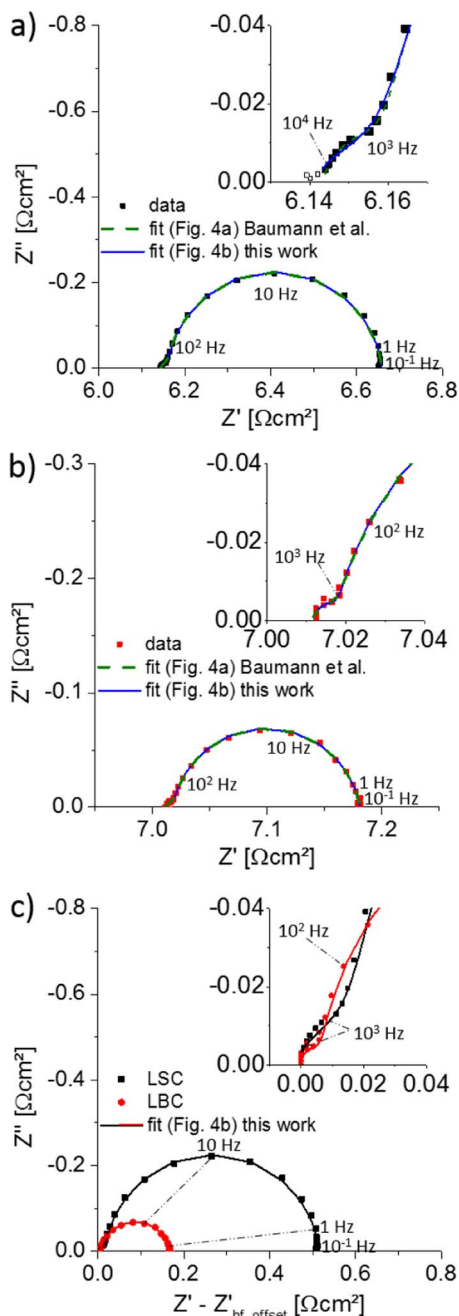


Figure 3. Nyquist plots of freshly deposited (a) LSC64 and (b) LBC64 thin films at $604 \pm 2^\circ\text{C}$ and 0.21 bar $p\text{O}_2$. Data points represent measured values and the solid lines the corresponding fits according to the model proposed by Baumann et al.¹¹ Fig. 4a and the model used in this work, Fig. 4b. The insets display the medium-low frequency (25 kHz–100 Hz) range for both materials. Fig. 3c shows a comparison of the two thin film materials after subtraction of the high frequency intercept.

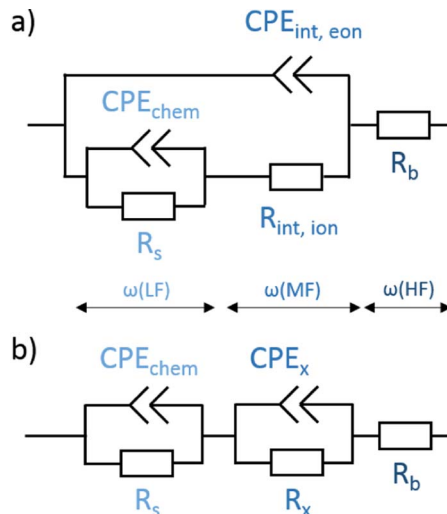


Figure 4. Equivalent circuit used to fit impedance data a) by Baumann et al.¹¹ for $\text{La}_{0.6}\text{Sr}_{0.4}\text{Co}_{0.8}\text{Fe}_{0.2}\text{O}_{3-\delta}$ thin films and b) for LSC64 thin films in this work.

materials is made in Fig. 3c after subtraction of the high frequency intercept. Qualitatively, both materials show a very similar Nyquist plot. The high-frequency intercept ($>25 \text{ kHz}$) on the x-axis can be predominantly attributed to the oxide ion conduction in the electrolyte. In addition, the high frequency intercept is slightly higher for the LBC sample, probably because of its smaller electronic conductivity compared to LSC (see Van der Pauw – electronic conductivity section), which may cause an additional sheet resistance. This additional high frequency resistance amounts to 13 – 18% of the total high frequency intercept and might indicate a slightly smaller active surface area for the LBC sample. However, compared to other effects found in this study, these differences are of minor importance and were thus not considered for the calculation of the resistive and capacitive values presented in this work. The electrode impedance is determined by a small shoulder at medium frequencies (25 kHz–1 kHz) and a pronounced low frequency (1 kHz–0.1 Hz) semicircle. It is generally agreed that the oxygen exchange resistance dominates the overall electrode impedance for thin films of the $\text{La}_{1-x}\text{Sr}_x\text{Co}_{1-y}\text{Fe}_y\text{O}_{3-\delta}$ perovskite family.^{40–43} Therefore, the resistive contribution of the low frequency semicircle is associated with the oxygen exchange reaction at the surface, which is also supported by its time, temperature and pressure dependency shown in the following sections. Accordingly, the surface exchange resistance can already be approximated from the impedance spectra without any detailed fit model.

A surface exchange resistance (R_{surf}) of $\sim 0.5 \text{ } \Omega\text{cm}^2$ is found for the freshly deposited LSC thin film, which is in good agreement with literature values^{31,34} reported for similarly prepared thin films. This indicates that, compared to other materials, already LSC thin films show excellent kinetics for the oxygen reduction reaction at 600°C ; other values are: $\text{Ba}_{0.6}\text{Sr}_{0.4}\text{Co}_{0.2}\text{Fe}_{0.8}\text{O}_{3-\delta}$ ⁴⁴ $\sim 3 \text{ } \Omega\text{cm}^2$, $\text{SrFeO}_{3-\delta}$ ⁴⁵ $\sim 9 \text{ } \Omega\text{cm}^2$, $\text{Sm}_{0.5}\text{Sr}_{0.5}\text{CoO}_{3-\delta}$ ⁴² $\sim 14 \text{ } \Omega\text{cm}^2$, $\text{La}_{0.6}\text{Sr}_{0.4}\text{Co}_{0.2}\text{Fe}_{0.8}\text{O}_{3-\delta}$ ⁴² $\sim 70 \text{ } \Omega\text{cm}^2$, $\text{SrTi}_{0.95}\text{Fe}_{0.05}\text{O}_{3-\delta}$ ⁴⁵ $\sim 85 \text{ } \Omega\text{cm}^2$, $\text{La}_{0.6}\text{Sr}_{0.4}\text{FeO}_{3-\delta}$ ⁴⁶ $\sim 130 \text{ } \Omega\text{cm}^2$. Freshly deposited LBC, however, shows an even lower surface exchange resistance than LSC; impressively small $\sim 0.17 \text{ } \Omega\text{cm}^2$ can be estimated, see Fig. 5. This is certainly among the lowest oxygen surface exchange resistances reported so far for dense perovskite-type materials and to the best of our knowledge also the first value reported for the oxygen exchange kinetics of dense LBC thin films.

One of the major challenges in impedance spectroscopy is the quantitative evaluation of spectra in order to extract physically meaningful quantities. In general, impedance analysis is performed using equivalent circuits that consist of a network of resistors and capacitors. For a detailed analysis of the electrode impedance in Fig. 3 two different equivalent circuit models, see Fig. 4, were employed to fit the data; CPE denotes constant phase elements.

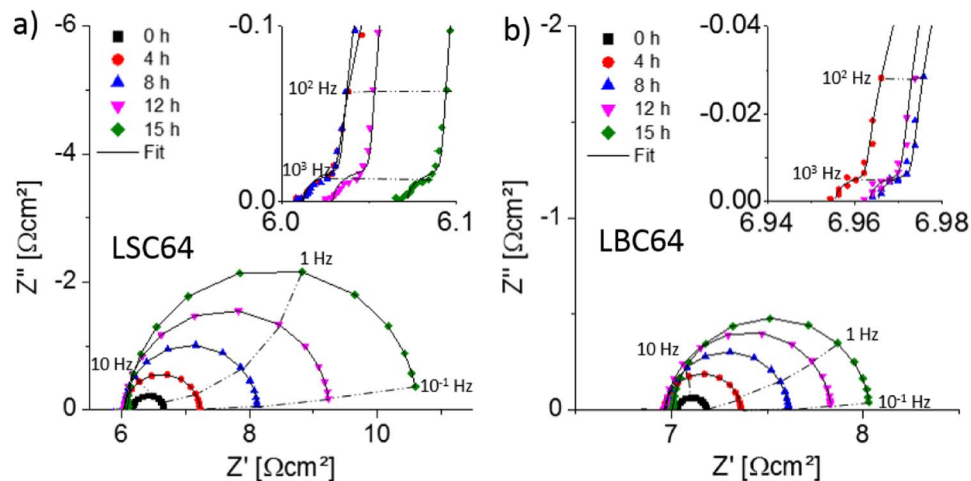


Figure 5. Nyquist plots displaying the impedance change of a LSC64 (a) and LBC64 (b) thin film upon annealing at 604°C and 0.21 bar pO₂. Data points represent measured values and the solid line is the corresponding fit according to the model presented in Fig 4b. The insets show the medium-low frequency (25 kHz–100 Hz) range.

It can be seen in Figs. 3a and 3b that both models describe the measured data quite well but an excellent agreement between the equivalent circuit and the experimental data does not necessarily confirm the validity of any model. For a physical interpretation it is important to check whether the values of the fitting parameters are reasonable and show the expected dependencies on temperature, oxygen partial pressure and geometrical variations.

Baumann et al.¹¹ already approached this issue for La_{0.6}Sr_{0.4}Co_{0.8}Fe_{0.2}O_{3-δ} (LSCF) thin films and derived the equivalent circuit shown in Fig. 4a from a general description of mixed ionic-electronic conductors proposed in Ref. 47 under the assumptions of a very high ionic and electronic conductivity i.e. the oxygen incorporation into the electrolyte $1/2O_{2, gas} + 2e^- \rightarrow O_{electrolyte}^{2-}$ is limited by the surface exchange and electrode-electrolyte interface transfer. In this model R_b represents the ionic bulk conductivity of the electrolyte, R_{int, ion} the oxygen transfer between electrode and electrolyte and R_s the surface exchange resistance. The capacitors were replaced by constant phase elements, where

$$Z_{CPE} = \frac{1}{Q(i\omega)^n} \quad [1]$$

is the impedance of the constant phase element and the capacitance is calculated by

$$C = (R^{1-n} \cdot Q)^{\frac{1}{n}} \quad [2]$$

For n = 1 the impedance of the constant phase element corresponds to the impedance of an ideal capacitor. CPE_{int, eon} represents the double layer capacitance expected at the interface between electrode and electrolyte due to the blockage of electronic charge carriers and C_{chem} the chemical capacitance of the thin film.

One may suggest the same equivalent circuit for our La_{0.6}Sr_{0.4}CoO_{3-δ} (LSC64) and La_{0.6}Ba_{0.4}CoO_{3-δ} (LBC64) thin films, since they also show an excellent mixed conductivity and are limited by the surface exchange reaction. However, inconsistencies with this model are found in the medium frequency regime (small shoulder), since the extracted values for an interfacial double layer capacitance are too large. Baumann¹¹ calculated a C_{int, eon} of ~100 μF/cm² for LSCF thin films at 500°C, while in our case much larger values are deduced from the model in Fig. 4a (LSC ~2500 μF/cm², LBC ~10000 μF/cm² for the two thin films at 510°C). Yang et al.⁴⁸ also measured similarly high capacitances in the medium frequency range on La_{0.5}Sr_{0.5}CoO_{3-δ} thin films. Assuming a capacitor thickness as small as the interatomic distance of the two cation layers in an elementary

cell (d = 1.9 Å), a relative permittivity ε_r can be calculated by

$$\epsilon_r = \frac{C_{int, eon}}{A} \cdot \frac{d}{\epsilon_0} \quad [3]$$

with ε₀ (= 8.85 · 10⁻¹² F/m) being the vacuum permittivity, and A the interfacial area. This model would deliver relative permittivity values of ~430 (LSC) and ~2100 (LBC). Such large ε_r values are hardly conceivable while the value of ~21 for LSCF, calculated using C_{int, eon} from Ref. 11, is still in a realistic range. Therefore, we suggest that the high capacitance obtained at medium frequencies in this work represents stoichiometric changes and thus also reflects a chemical capacitance. Hence, it is not appropriate to use the Baumann model (Fig. 4a), since a second chemical capacitance would rather be in series and not in parallel to the R_s||CPE_{chem} element. Quantities discussed in this work are thus extracted by the modified equivalent circuit shown in Fig. 4b. The exact mechanisms behind CPE_x and R_x are unknown and the circuit is considered as approximation of a more complex one; values could only be determined with limited accuracy, since the overall electrode impedance is strongly dominated by the large arc, i.e. by CPE_{chem} and R_s. Exponential fitting parameters of n ~0.7 for the R_x||CPE_x and n > 0.92 for the R_s||CPE_{chem} element were determined throughout this work.

EIS - Time dependent measurements.—Electrochemical impedance spectroscopy was used to investigate changes of the electrochemical performance for as-deposited LSC and LBC thin film electrodes at 604 ± 2°C in synthetic air (0.21 bar pO₂) over annealing time. Impedance spectra were measured continuously in an interval of ~5 minutes for 15 hours. Nyquist plots normalized to the projected electrode surface area are shown in Fig. 5a for LSC and Fig. 5b for LBC thin films after the given annealing times. The points represent measured data and the straight line the fit according to the model shown in Fig. 4b.

Figs. 6a and 6b summarize the resistive and capacitive changes during 15 hours of annealing. The oxygen surface exchange resistance R_s increases continuously from 0.5 Ωcm² to 4.2 Ωcm² for LSC and 0.15 Ωcm² to 1 Ωcm² for LBC within 15 hours of annealing time at 600°C. The degradation of the electrochemical exchange kinetics of LSC and related materials was often reported and mostly connected to cation stoichiometry changes at or close to the surface.⁴⁹⁻⁵¹ Especially, the presence of certain atmospheric trace gases such as SO₂, CO₂ or H₂O⁵²⁻⁵⁴ as well as Si or Cr sources in the vicinity of perovskite samples in wet atmosphere are known to decrease the electrode performance by formation of Sr rich phases on the surface.^{55,56} Even though similar degradation mechanisms may affect thin film

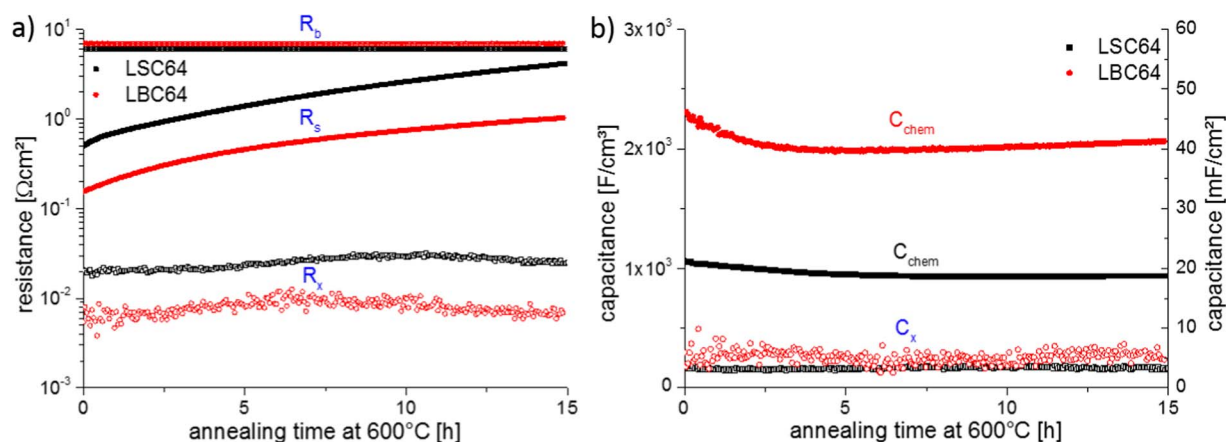


Figure 6. Variation of the (a) resistive and (b) capacitive quantities of LSC64 and LBC64 thin films with annealing time at 600°C and 0.21 bar pO₂. All values are normalized to the projected surface area (R_s , R_x , R_b , C_x) or the film volume (C_{chem}).

electrodes as well as macroscopic electrodes we generally found that degradation rates are faster for thin films. However, special care was attributed to avoiding any contaminations of the atmosphere during the annealing procedure, see Electrochemical measurements section. For similarly prepared LSC thin films we already showed by low-energy ion sputtering and on-line inductively coupled plasma mass spectrometry³¹ that degradation during annealing (in the same setup) is not necessarily connected to severe cation stoichiometry changes at the surface. It is beyond the scope of this paper to clarify reasons of the changes measured here but they have to be kept in mind when analyzing activation energies (EIS - Temperature dependent measurements section).

C_{chem} decreases within the first 5 hours from 1050 Fcm⁻³ to 950 Fcm⁻³ for LSC and from 2300 Fcm⁻³ to 2000 Fcm⁻³ for LBC. This minor variation may be due to morphological changes of the thin film since the samples were only shortly at such temperatures during deposition (20 minutes). The higher C_{chem} values for LBC reflects its ability to undergo larger stoichiometric changes upon polarization in comparison to LSC. For C_x , measured at medium frequencies, very high values in the order of 4 to 7 mF/cm² were obtained. Neither C_x nor R_x show substantial changes with annealing time for both materials; R_x is 1–2 orders of magnitude smaller than R_s at the start of the measurement. For both materials R_b remains the same and is close to the expected value assuming a YSZ ionic conductivity of $4.75 \cdot 10^{-3}$ S/cm at 600°C.

EIS - Temperature dependent measurements.—Freshly deposited LSC and LBC thin films were thermally equilibrated in synthetic air at 604°C for 1 h and then measured between 604°C and 463°C with

intervals of 22–24°C. A total of 8 temperature cycles (each consisting of 1 heating and 1 cooling subcycle) was measured for both materials with each temperature cycle taking approx. 8 hours. Representative Nyquist plots at different temperatures during the first temperature cycle are shown in Fig. 7. A very good agreement between equivalent circuit fit (solid line) and measured data (points) is found over the whole temperature range. The general shape of the impedance spectra at medium and low frequencies does not change at lower temperatures. However, at higher frequencies (> 10 kHz) the onset of a semicircle is observed, which represents the ionic resistance of the YSZ electrolyte in parallel to its geometrical capacitance. This part of the spectra was not visible at 604°C, because of the higher bulk relaxation frequency which is proportional to the ionic conductivity. The higher R_b value found for the LBC sample may be again attributed to a sheet resistance and thus slightly decreased active area of the electrode. Arrhenius plots of the resistances and capacitances extracted from the first temperature cycle together with their activation energies are shown in Fig. 8. For all quantities, except C_x of LBC, an Arrhenius-type behavior could be determined. The activation energies obtained for $1/R_b$, for example, are 1.02 ± 0.01 eV for LSC and 1.04 ± 0.01 eV for LBC, and agree well with literature values reported for the ionic bulk conductivity of 9.5 mol% YSZ single crystals, 1.07 ± 0.06 eV.^{11,48,57,58}

The activation energy of the oxygen surface exchange is 1.26 ± 0.02 eV for LSC and 1.19 ± 0.11 eV for LBC, calculated from all data of the first temperature cycle. However, as already mentioned in EIS - Time dependent measurements section degradation occurs, leading to an increase of the surface exchange resistance with annealing time also during the temperature cycles, see Fig. 9a. The increase of the absolute values is accompanied by a continuous increase of the

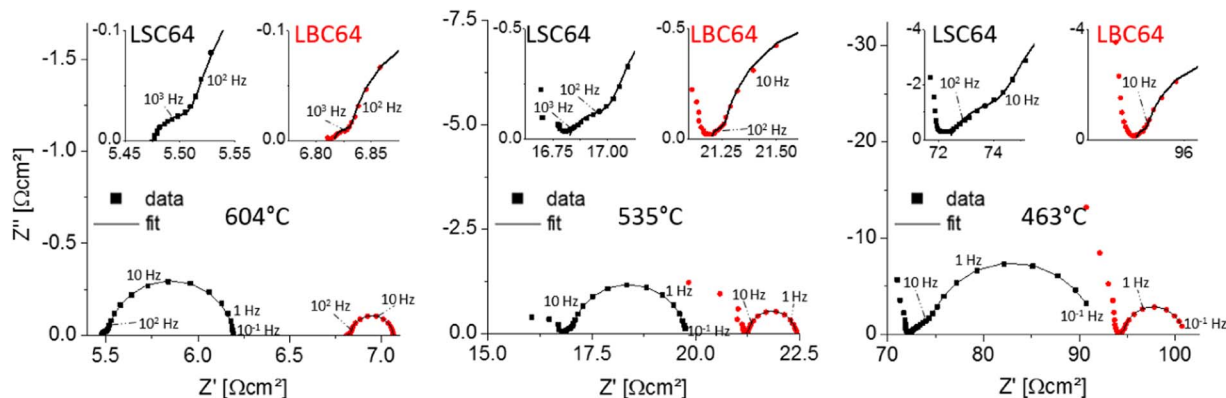


Figure 7. Nyquist plots displaying the dependence of the (a) LSC64 and (b) LBC64 thin films on temperature at 0.21 bar pO₂. Data points represent measured values and the solid line the corresponding fit according to the model presented in Fig 4b. The insets show the medium-low frequency (25 kHz–100 Hz) range for both materials.

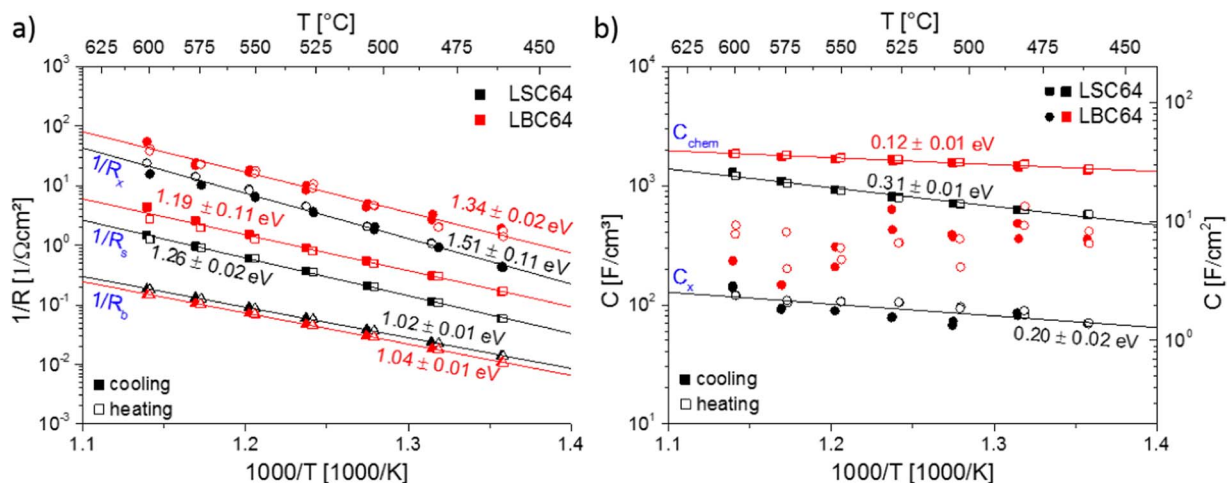


Figure 8. Arrhenius plots of the (a) resistive and (b) capacitive quantities of LSC64 and LBC64 thin films at 0.21 bar p_{O_2} measured during the first cooling (■) and heating (□) subcycle. The activation energies determined from these data are also given.

activation energy with number of temperature cycles, as can be seen in Fig. 9b. The activation energy calculated from the last (8th) temperature cycle amounts to 1.33 ± 0.04 eV for LSC and 1.33 ± 0.02 eV for LBC. The surface exchange resistance continuously increases during the temperature cycles. Therefore, the activation energy is shifted to lower values when calculated from a heating subcycle only and to higher values when calculated from a cooling subcycle. The averaged activation energies are shown in Fig. 9b by a polynomial approximation.

For both materials a similar pre-exponential factor of the Arrhenius equation, $5 \cdot 10^{-8} \pm 2 \cdot 10^{-8} \Omega\text{cm}^2$ for LSC and $4 \cdot 10^{-8} \pm 3 \cdot 10^{-8} \Omega\text{cm}^2$ for LBC, is found. Hence, the different oxygen exchange kinetics of the two materials can be mainly attributed to the different activation energies. Moreover, the pre-exponential factor changes by less than 10% during the course of the 8 temperature cycles. This factor includes the high temperature limit of the number of sites participating in the rate limiting step of the oxygen exchange reaction. Even without exact knowledge of the nature of those sites it is reasonable to conclude from this constancy that only a small fraction of possible reaction sites becomes deactivated during the course of the measurements. Thus, mainly the change of the activation energy causes degradation. This change may reflect a homogenous and continuous variation of the chemical environment of active surface sites.

However, for LSC and most other MIECs it is still under debate, which elementary step is rate limiting during the oxygen incorporation i.e. adsorption, dissociation, charge transfer. Hence, it is also difficult to find a more detailed explanation for the degradation. Regardless of the drifting activation energy, it has to be emphasized that both, LSC and LBC, show very low activation energies for the oxygen incorporation compared to other MIEC perovskite-type materials. This makes both of them and especially LBC due to its low absolute polarization resistance highly attractive for the use in intermediate-temperature SOFCs.

For the unknown interfacial process, represented by R_x , an activation energy of 1.51 ± 0.11 eV for LSC and 1.34 ± 0.02 eV for LBC was calculated. As already discussed in Electrochemical measurements section, Baumann et al. assigned this resistive contribution to the transfer of O^{2-} ions across the electrode/electrolyte boundary and determined an activation energy of 1.55 ± 0.05 eV for $\text{La}_{0.6}\text{Sr}_{0.4}\text{Co}_{0.8}\text{Fe}_{0.2}\text{O}_{3-\delta}$ thin films.¹¹ Yang et al. assumed a similar reaction mechanism for the medium frequency range and obtained an activation energy of 1.6 eV for $\text{La}_{0.5}\text{Sr}_{0.5}\text{CoO}_{3-\delta}$ thin films.⁴⁸ A more detailed discussion of this minor part to the overall polarization resistance is beyond the scope of this paper.

Fig. 8b shows the activation energies of C_{chem} for LSC (0.31 ± 0.01 eV) and LBC (0.12 ± 0.01 eV). C_{chem} is proportional to $\partial\delta/\partial\mu_{O_2}$,

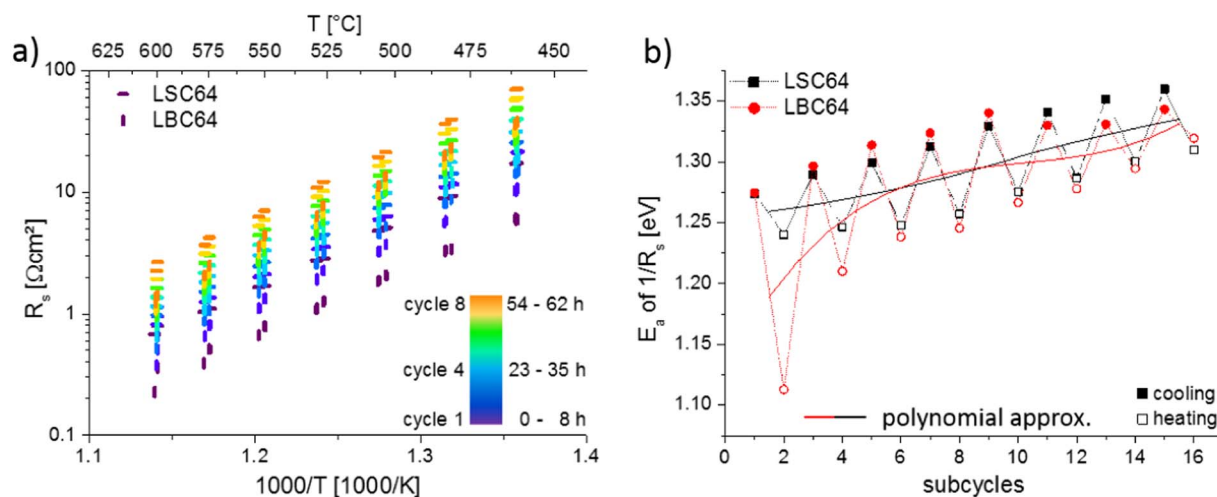


Figure 9. (a) Arrhenius plot of the surface exchange resistance of LSC64 and LBC64 thin films at 0.21 bar p_{O_2} . For each thin film 8 temperature cycles (cooling and heating) were performed within 62 hours. (b) The activation energies of $1/R_s$ calculated from each subcycle of (a) and a polynomial approximation is shown (solid line).

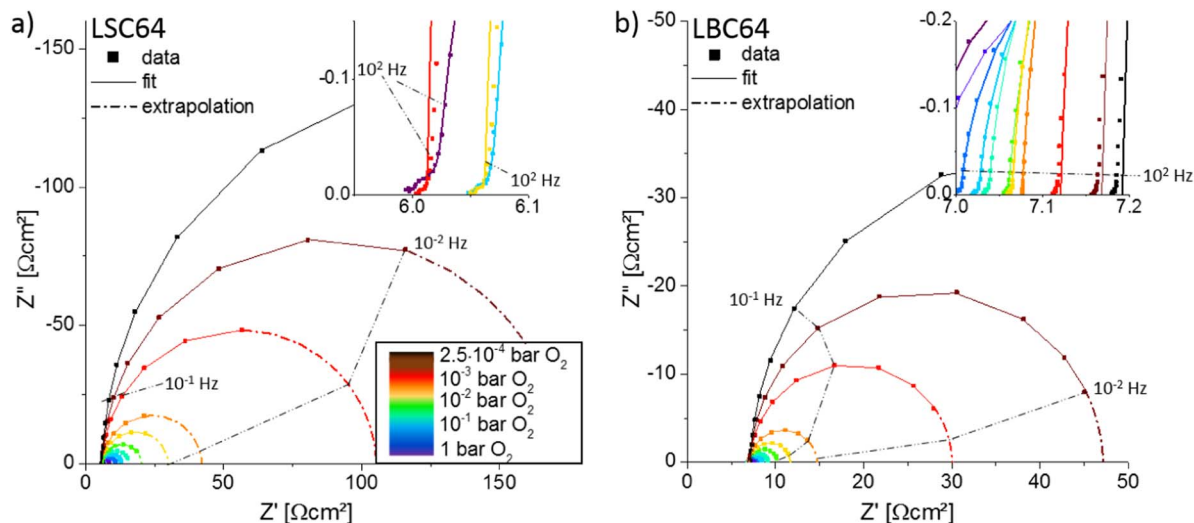


Figure 10. Nyquist plots displaying the dependence of the LSC64 and LBC64 thin film impedance on pO_2 at $600^\circ C$. Data points represent measured values and the solid line the corresponding fit according to the model presented in Fig 4b. The insets show the medium-low frequency (25 kHz–100 Hz) range for both materials. For a better overview, only a limited selection of graphs is displayed in the inset of (a).

with μ_O being the chemical potential of oxygen in the electrode. Thus, a positive activation energy is in accordance with data obtained by coulometric titration⁵⁹ and thermogravimetry⁶⁰ for polycrystalline $La_{0.6}Sr_{0.4}CoO_{3-\delta}$ and $La_{0.7}Sr_{0.3}CoO_{3-\delta}$ bulk samples respectively. A detailed discussion of C_{chem} and a comparison to literature values is given in EIS – pO_2 dependent measurements section. For LBC a clear trend of the temperature dependence of C_x could not be observed. However, for the LSC thin films an activation energy of 0.20 ± 0.02 eV was determined. The positive activation energy again highlights the difference to the interfacial capacitance reported in Ref. 11 for $La_{0.6}Sr_{0.4}Co_{0.8}Fe_{0.2}O_{3-\delta}$ thin films, the latter is negatively thermally activated by -0.15 ± 0.05 eV.

EIS – pO_2 dependent measurements.—Subsequent to the time dependent measurements, see EIS - Time dependent measurements section, EIS analysis was performed on both materials at constant temperature ($604^\circ C$) but different atmospheres. The ratio of the O_2/N_2 gas mixture was changed using mass flow controllers to vary the oxygen partial pressure (pO_2) between 1 and $2.1 \cdot 10^{-4}$ bar pO_2 . A pO_2 cycle from 0.21 to $2.1 \cdot 10^{-4}$ and back to 1 bar pO_2 was recorded for both materials within 10 hours. Qualitatively, degradation slowed down at lower oxygen partial pressures and therefore values obtained during the decreasing and increasing pO_2 subcycle are in good accordance. In Fig. 10 Nyquist plots are shown for the whole oxygen partial pressure range and both materials. It can be seen that the fit becomes less accurate in the medium frequency range for measurements performed at lower oxygen partial pressures ($\leq 10^{-2}$ bar pO_2), see insets in Figs. 10a and 10b. Therefore, it was not possible to extract the quantities R_x and C_x for LBC at oxygen partial pressures below $5 \cdot 10^{-2}$ bar pO_2 . These deviations, however, do not affect the much larger quantities R_s and C_{chem} .

Moreover, some minor dependence of the high frequency intercept on pO_2 was observed for both samples. While for the LSC sample the changes can be most probably attributed to small temperature fluctuations due to different gas fluxes, the high frequency intercept of the LBC samples systematically increases with decreasing pO_2 . Under equilibrium conditions oxygen is removed from the electrode bulk at lower oxygen partial pressures. According to the reaction $O_x \rightleftharpoons 1/2 O_2 + 2e^- + V_O^\bullet$ electrons are left behind in the electrode. Those recombine with holes $h^+ + e^- \rightleftharpoons nil$ and this usually decreases the conductivity of a p-type material. Hence, for the slightly less conductive LBC (see below) an increase of the already existing sheet

resistance may cause the shift of the high frequency intercept, R_b , with decreasing pO_2 .

The oxygen surface exchange resistance exhibits a power law behavior $R_s \sim (pO_2)^m$ for $pO_2 < 5 \cdot 10^{-2}$ bar. For both materials, exponents m between -0.65 to -0.68 are found. At higher pressures the pO_2 dependence becomes very weak. This is most probably not caused by a change of the rate limiting step to ionic transport; a change of the impedance shape from a semicircle to a Warburg element is not observed and the exponential fitting parameter n of the CPE elements was >0.98 at 1 bar pO_2 . The very similar pO_2 dependence of R_s for LSC and LBC again support the assumption that the oxygen reduction mechanism and rate limiting step are the same and only differ in their activation energy. However, a detailed mechanistic interpretation of the pO_2 dependence is far from trivial since pO_2 not only affects the concentration of adsorbed species but also all defect concentrations in the MIEC. Such a defect chemical analysis is beyond the scope of this work. R_x exhibits large fitting errors of approx. 30–80% for both materials and does not show a clear dependence on the oxygen partial pressure. Also the step change of R_x in Fig. 9a between $1 \cdot 10^{-2}$ and $2 \cdot 10^{-2}$ bar pO_2 for LSC most probably originates from fit inaccuracies.

Fig. 10b shows that C_{chem} and C_x of both materials decrease with increasing oxygen partial pressure, which supports the assumption of C_x also being a chemical capacitance (of the interface). C_{chem} of LBC is larger than for LSC over the measured partial pressure range but the difference decreases toward lower pO_2 . The larger C_{chem} of LBC indicates that the material is more ready for stoichiometry changes, i.e. is easier to reduce compared to LSC. This may be due to the fact that the larger ionic radius of Ba leads to an increased lattice parameter, as shown in Structural characterization section, and thereby offers more space to form oxygen vacancies and reduced (larger) B cations.⁶¹ A similar observation was made on $Ba_xSr_{1-x}Ti_{1-y}Fe_yO_{3-\delta}$ bulk samples using thermogravimetry to analyze the oxygen vacancy concentration.^{22,23} It was found that the non-stoichiometry curve is shifted to higher pO_2 with higher amounts of Ba. In analogy, we may assume that the LBC- C_{chem} curve in Fig. 11b is shifted compared to LSC by about 3–4 orders of magnitude in pO_2 and thus that LBC has a higher vacancy concentration due a lower vacancy formation enthalpy. Unfortunately, C_{chem} cannot be used to directly determine the concentration of oxygen vacancies, which are the minority charge carriers in the measured pO_2 range, since we do not fulfil the prerequisite of a dilute system to apply the corresponding simplified equations.⁴⁷

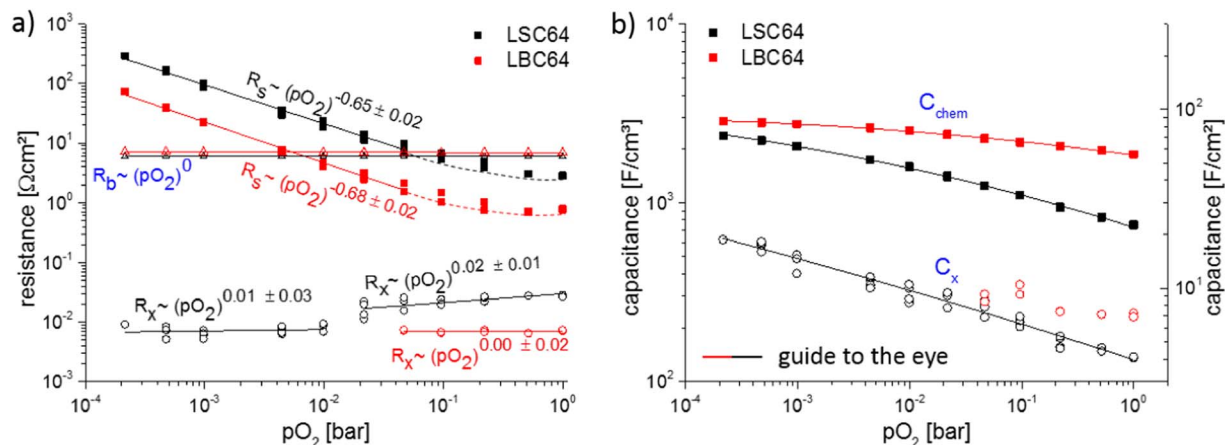


Figure 11. Dependence of the (a) resistive and (b) capacitive quantities of LSC64 and LBC64 thin films on pO_2 at 600°C. Power laws according to $R_s \sim (pO_2)^m$ are highlighted together with their linear fit (solid lines) in (a). The solid lines in (b) represent a guide to the eye.

Nonetheless, we may compare the measured chemical capacitances of LSC with those expected from non-stoichiometry data of bulk samples. The chemical capacitance is given by

$$C_{chem} = \frac{4 \cdot F^2 d (3 - \delta)}{V_M d\mu_o} \quad [4]$$

with F being the Faraday constant ($96485 \text{ C} \cdot \text{mol}^{-1}$) and V_M denoting the molar volume of LSC64 ($39.12 \text{ cm}^3 \cdot \text{mol}^{-1}$). The non-stoichiometry data from Lankhorst et al.,⁶² Kawada et al./Mizusaki et al.^{60,63} and Kuhn et al.⁶⁴ for bulk samples were numerically evaluated in terms of Eq. 4. The resulting C_{chem} values are plotted in Fig. 12 together with C_{chem} values directly obtained from the impedance measurements in our study but also from measurements on thin films by Kawada²³ and Yang ($\text{La}_{0.5}\text{Sr}_{0.5}\text{CoO}_{3-\delta}$)⁴⁸ at 600°C and different oxygen partial pressures. It can be seen that our data fit rather well to the bulk based models from Lankhorst, Kawada/Mizusaki and Kuhn, C_{chem} values of the three latter deviate from each other by less than 50%. In contrast to this, the C_{chem} values extracted from

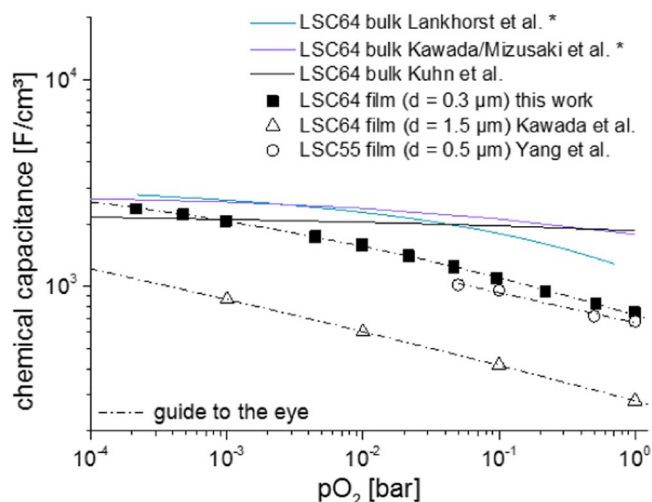


Figure 12. Dependence of the chemical capacitance on pO_2 at 600°C for LSC64 and LSC55, respectively. Data determined from $\delta(\mu_o)$ slopes of thermogravimetry and coulometric titration measurements by Lankhorst,⁶² Kawada/Mizusaki^{60,63} and Kuhn⁶⁴ on bulk samples (solid line) are shown together with data extracted from impedance measurements on thin films by Kawada²³ and Yang⁴⁸ (open symbols). The asterisk (*) denotes that data had to be extrapolated, d is the thickness of the thin films. A dashed line is drawn as guide to the eye.

thin films on $\text{Ce}_{0.9}\text{Gd}_{0.1}\text{O}_{1.95}$ (GDC) by Kawada⁶³ are a factor of 2–3 lower. Possibly epitaxial growth of LSC64 on top of GDC restricts chemical expansion of the LSC layer i.e. formation of oxygen vacancies while expansion restriction from the substrate is less pronounced in our thin films. Our measured data are therefore only slightly shifted to lower oxygen partial pressures compared to bulk data.

Van der Pauw – electronic conductivity.—Resistivity measurements using the van der Pauw method³² were performed on LSC and LBC thin films at 0.21 bar pO_2 and different temperatures (80–600°C). This technique is able to determine the thin film resistivity irrespective of the contact placement and the shape of the sample (as long as point contacts are at the periphery of the specimen). To ensure that the YSZ substrate does not influence the thin film conductivity measurement, the conductivity of YSZ obtained during the impedance measurement at 600°C, $4.75 \cdot 10^{-3} \text{ S/cm}$, is used to compare sheet resistances of substrate and film. From $R_{sheet} = \frac{1}{\sigma \cdot d}$, with d being the thickness, the measured sheet resistance of the thin film is in the 1% range of the substrate sheet resistance and thus a substrate effect can be safely neglected.

The temperature dependent electronic conductivity resulting after one hour thermal equilibration at 600°C is shown in Fig. 13 for both materials. LSC is known to be primarily electron conducting under these conditions and also LBC thin films revealed conductivity values far above any conceivable ionic conductivity. The samples were equilibrated for 1 hour at 600°C before several temperature cycles were started. In Fig. 13a it can be seen that for both materials a conductivity maximum is found (LSC $\sigma_{eon} = 1028 \text{ S/cm}$ at $382 \pm 8^\circ\text{C}$, LBC 839 S/cm at $442 \pm 5^\circ\text{C}$). At higher temperatures, σ_{eon} decreases as one would expect for metallic conductivity. The maximum of σ_{eon} for LSC is observed close to the phase transition temperature of $\sim 390^\circ\text{C}$ for bulk samples, where the crystal lattice changes from the low temperature rhombohedral into a cubic structure. However, for bulk LSC64 samples the maximum of σ_{eon} was found to be close to 0°C ¹⁵. A hysteresis like behavior is measured for the LBC sample for yet unknown reasons.

In Fig. 13b additional measurements from Ding et al.⁶⁵ and Mizusaki et al.¹⁵ on LSC64 and LSC73 bulk samples, respectively, are plotted together with LSC64 thin film measurements conducted by Joo et al.⁶⁶ While the thin film data of Joo and our work correspond well, a difference of about 40% is found between thin film and bulk samples. This could again be caused by defect chemical differences between bulk and thin film but might also be due to the columnar microstructure of our thin films, since the grain boundaries may have a higher resistivity. The somewhat smaller electronic conductivity of LBC was already mentioned in EIS – Initial measurements and

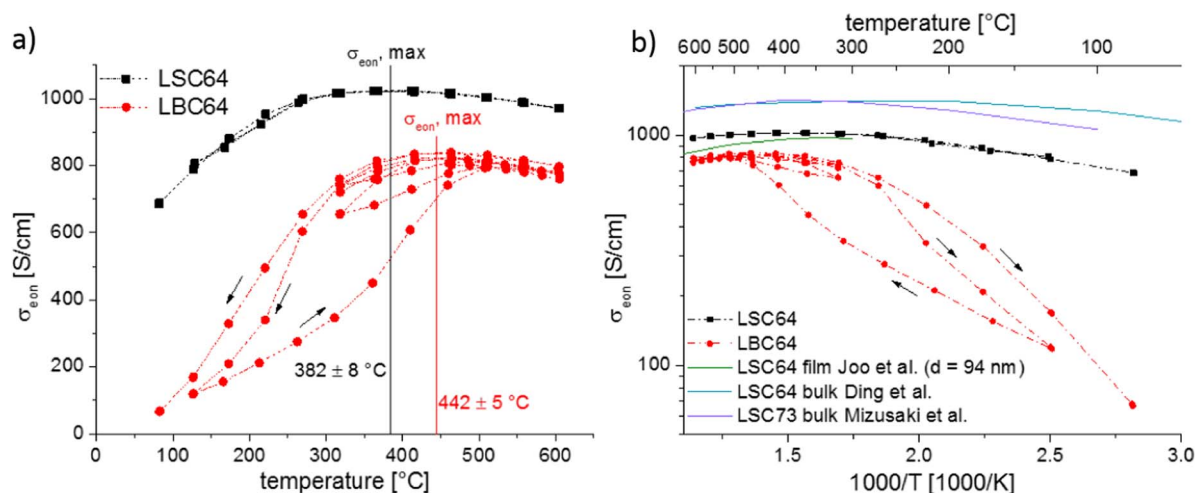


Figure 13. Electronic conductivity measured by van der Pauw method for LSC64 and LBC64 thin films at different temperatures and 0.21 bar pO₂ in linear (a) and logarithmic (b) plots; dashed lines serve as guide to the eye. Literature data measured on bulk samples by Ding⁶⁵ and Mizusaki¹⁵ are also plotted as reference in (b).

equivalent circuit model section as the possible cause of an increased high frequency intercept. However, above 400°C the conductivity is still far beyond that of most SOFC cathode materials such as La_{1-x}Sr_xMnO_{3-δ} and La_{1-x}Sr_xFeO_{3-δ} and sufficient for excellent cathodes. Hence, we conclude that based on its superior oxygen exchange activity LBC is a highly promising material for porous cathodes in intermediate temperature SOFCs.

Conclusions

This work revealed the extraordinarily high catalytic activity of dense La_{0.6}Ba_{0.4}CoO_{3-δ} (LBC) thin film model electrodes for the oxygen surface exchange. A comparative study with La_{0.6}Sr_{0.4}CoO_{3-δ} (LSC) thin films showed that the oxygen incorporation of both perovskite-type material is limited by the oxygen surface exchange reaction in the temperature range of 450–600°C. The surface exchange resistance R_s in synthetic air, already known to be very low for LSC (0.5–0.7 Ωcm² at 604°C, 17–18 Ωcm² at 463°C) is even lower for LBC (0.15–0.22 Ωcm² at 604°C, 5.8–6 Ωcm² at 463°C). Furthermore, a very low activation energy of R_s was found for both materials (LSC 1.26 ± 0.11 eV, LBC 1.19 ± 0.11 eV) in the temperature range relevant for intermediate temperature SOFC applications.

A very similar oxygen partial pressure dependency of the surface exchange resistance was found for both materials and together with other similarities this suggests the same oxygen incorporation mechanism. Differences and variations of R_s are mainly caused by changes of the activation energy. The larger chemical capacitance of LBC is attributed to an increased reducibility of the perovskite lattice caused by the introduction of the larger Ba ion in comparison to Sr. Chemical capacitances of LSC films are close to those expected from bulk defect chemical data. The temperature dependence of the electronic conductivity revealed a maximum for LSC σ_{eon} = 1028 S/cm at 382 ± 8°C and LBC 839 S/cm at 442 ± 5°C. At all relevant temperatures, conductivity values are by far sufficient for application in SOFCs.

Acknowledgment

The authors gratefully acknowledge funding by Austrian Science Fund (FWF) project P4509-N16 and W1243-N16.

References

- J. W. Fergus, *Solid State Ionics*, **177**(17–18), 1529 (2006).
- K. Eguchi, H. Kojo, T. Takeguchi, R. Kikuchi, and K. Sasaki, *Solid State Ionics*, **152** 411 (2002).
- A. B. Stambouli and E. Traversa, *Renewable and Sustainable Energy Reviews*, **6**(5), 433 (2002).
- Z. Shao and S. M. Haile, *Nature*, **431**(7005), 170 (2004).
- S. Jiang and S. Chan, *Journal of Materials Science*, **39**(14), 4405 (2004).
- W. Quadakkers, J. Piron-Abellan, V. Shemet, and L. Singheiser, *Materials at high temperatures*, **20**(2), 115 (2003).
- S. C. Singhal and K. Kendall, *High-temperature solid oxide fuel cells: fundamentals, design and applications: fundamentals, design and applications*, Elsevier (2003).
- E. D. Wachsman and K. T. Lee, *Science*, **334**(6058), 935 (2011).
- A. Tarancón, M. Burriel, J. Santiso, S. J. Skinner, and J. A. Kilner, *Journal of Materials Chemistry*, **20**(19), 3799 (2010).
- D. J. Brett, A. Atkinson, N. P. Brandon, and S. J. Skinner, *Chemical Society Reviews*, **37**(8), 1568 (2008).
- F. S. Baumann, J. Fleig, H. Habermeier, and J. Maier, *Solid State Ionics*, **177**(11–12), 1071 (2006).
- S. B. Adler, *Chemical reviews*, **104**(10), 4791 (2004).
- C. Endler-Schuck, in "Schriften des Instituts für Werkstoffe der Elektrotechnik", Vol. PhD, p. 187. Karlsruhe Institut für Technologie, Karlsruhe, 2011.
- M. Kuhn, Y. Fukuda, S. Hashimoto, K. Sato, K. Yashiro, and J. Mizusaki, *Journal of The Electrochemical Society*, **160**(1), F34 (2013).
- J. Mizusaki, J. Tabuchi, T. Matsuura, S. Yamauchi, and K. Fueki, *Journal of The Electrochemical Society*, **136**(7), 2082 (1989).
- J. W. Stevenson, T. R. Armstrong, R. D. Carneim, L. R. Pederson, and W. J. Weber, *Journal of The Electrochemical Society*, **143**(9), 2722 (1996).
- Y. Shao-Horn, *Journal of The Electrochemical Society*, **156**(7), B816 (2009).
- J. Mizusaki, T. Sasamoto, W. R. Cannon, and H. Bowen, *Journal of the American Ceramic Society*, **66**(4), 247 (1983).
- K. Yashiro, I. Nakano, M. Kuhn, S. Hashimoto, K. Sato, and J. Mizusaki, *ECS Transactions*, **35**(1), 1899 (2011).
- J. A. Kilner, R. A. De Souza, and I. C. Fullarton, *Solid State Ionics*, **86–88**, Part 2, 703 (1996).
- R. Shannon, *Acta Crystallographica Section A*, **32**(5), 751 (1976).
- J. J. Kim, M. Kuhn, S. R. Bishop, and H. L. Tuller, *Solid State Ionics*, **230**, 2 (2013).
- M. Kuhn, J. J. Kim, S. R. Bishop, and H. L. Tuller, *Chemistry of Materials*, **25**(15), 2970 (2013).
- M. Koyama, C. j. Wen, and K. Yamada, *Journal of The Electrochemical Society*, **147**(1), 87 (2000).
- R. Amin and K. Karan, *Journal of The Electrochemical Society*, **157**(2), B285 (2010).
- C. Setevich, F. Prado, and D. Z. de Florio, *International Journal of Hydrogen Energy*, **39**(16), 8738 (2014).
- C. Setevich, L. Mogni, A. Caneiro, and F. Prado, *Journal of The Electrochemical Society*, **159**(1), B72 (2011).
- T. Ishihara, S. Fukui, H. Nishiguchi, and Y. Takita, *Solid State Ionics*, **152–153**, 609 (2002).
- S. Pang, X. Jiang, X. Li, Q. Wang, and Z. Su, *International Journal of Hydrogen Energy*, **37**(3), 2157 (2012).
- M. P. Pechini, (S. E. Co, ed.), Vol. US3330697 A, USA, 1967.
- G. M. Rupp, H. Tellez, J. Druce, A. Limbeck, T. Ishihara, J. Kilner, and J. Fleig, *Journal of Materials Chemistry A*, **3**(45), 22759 (2015).
- L. J. van der Pauw, *Philips Res. Rep.*, **13**, 1 (1958).
- P. Plonczak, A. Bieberle-Hütter, M. Søgaard, T. Ryll, J. Martynczuk, P. V. Hendriksen, and L. J. Gauckler, *Advanced Functional Materials*, **21**(14), 2764 (2011).
- G. M. Rupp, A. Limbeck, M. Kubicek, A. Penn, M. Stoger-Pollach, G. Friedbacher, and J. Fleig, *Journal of Materials Chemistry A*, **2**(19), 7099 (2014).
- H. Ullmann, N. Trofimenko, F. Tietz, D. Stöver, and A. Ahmad-Khanlou, *Solid State Ionics*, **138** (1–2), 79 (2000).

36. A. J. Jacobson, *Chemistry of Materials*, **22**(3), 660 (2009).
37. D. Garces, C. F. Setevich, A. Caneiro, G. J. Cuello, and L. Moggi, *Journal of Applied Crystallography*, **47**(1), 325 (2014).
38. S.-i. Hashimoto, Y. Fukuda, M. Kuhn, K. Sato, K. Yashiro, and J. Mizusaki, *Solid State Ionics*, **186**(1), 37 (2011).
39. V. M. Goldschmidt, *Naturwissenschaften*, **14**(21), 477 (1926).
40. G. J. la O' and Y. Shao-Horn, *Journal of The Electrochemical Society*, **156**(7), B816 (2009).
41. J. R. Wilson, M. Sase, T. Kawada, and S. B. Adler, *Electrochemical and Solid-State Letters*, **10**(5), B81 (2007).
42. F. S. Baumann, J. Fleig, G. Cristiani, B. Stuhlhofer, H.-U. Habermeier, and J. Maier, *Journal of The Electrochemical Society*, **154**(9), B931 (2007).
43. M. Kubicek, T. M. Huber, A. Welzl, A. Penn, G. M. Rupp, J. Bernardi, M. Stöger-Pollach, H. Hutter, and J. Fleig, *Solid State Ionics*, **256**(0), 38 (2014).
44. F. S. Baumann, J. Fleig, H. U. Habermeier, and J. Maier, *Solid State Ionics*, **177**(35–36), 3187 (2006).
45. W. Jung and H. L. Tuller, *ECS Transactions*, **35**(1), 2129 (2011).
46. S. Kogler, A. Nennung, G. M. Rupp, A. K. Opitz, and J. Fleig, *Journal of The Electrochemical Society*, **162**(3), F317 (2015).
47. J. Jammik and J. Maier, *Physical Chemistry Chemical Physics*, **3**(9), 1668 (2001).
48. Y. L. Yang, C. L. Chen, S. Y. Chen, C. W. Chu, and A. J. Jacobson, *Journal of The Electrochemical Society*, **147**(11), 4001 (2000).
49. E. J. Crumlin, E. Mutoro, Z. Liu, M. E. Grass, M. D. Biegalski, Y.-L. Lee, D. Morgan, H. M. Christen, H. Bluhm, and Y. Shao-Horn, *Energy & Environmental Science*, **5**(3), 6081 (2012).
50. S. P. Simner, M. D. Anderson, M. H. Engelhard, and J. W. Stevenson, *Electrochemical and Solid-State Letters*, **9**(10), A478 (2006).
51. Z. Cai, M. Kubicek, J. Fleig, and B. Yildiz, *Chemistry of Materials*, **24**(6), 1116 (2012).
52. E. Bucher, C. Gspan, F. Hofer, and W. Sitte, *Solid State Ionics*, **238**(0), 15 (2013).
53. E. Bucher, A. Egger, G. B. Caraman, and W. Sitte, *Journal of The Electrochemical Society*, **155**(11), B1218 (2008).
54. Y. Yu, H. Luo, D. Cetin, X. Lin, K. Ludwig, U. Pal, S. Gopalan, and S. Basu, *Applied Surface Science*, **323**(0), 71 (2014).
55. E. Bucher, M. Yang, and W. Sitte, *Journal of The Electrochemical Society*, **159**(5), B592 (2012).
56. E. Bucher, W. Sitte, F. Klauser, and E. Bertel, *Solid State Ionics*, **208**(0), 43 (2012).
57. M. Gerstl, E. Navickas, G. Friedbacher, F. Kubel, M. Ahrens, and J. Fleig, *Solid State Ionics*, **185**(1), 32 (2011).
58. P. S. Manning, J. D. Sirman, R. A. De Souza, and J. A. Kilner, *Solid State Ionics*, **100**(1–2), 1 (1997).
59. W. Sitte, E. Bucher, and W. Preis, *Solid State Ionics*, **154–155**, 517 (2002).
60. J. Mizusaki, Y. Mima, S. Yamauchi, K. Fueki, and H. Tagawa, *Journal of Solid State Chemistry*, **80**(1), 102 (1989).
61. D. Marrocchelli, S. R. Bishop, H. L. Tuller, and B. Yildiz, *Advanced Functional Materials*, **22**(9), 1958 (2012).
62. M. H. Lankhorst, H. Bouwmeester, and H. Verweij, *Journal of Solid State Chemistry*, **133**(2), 555 (1997).
63. T. Kawada, J. Suzuki, M. Sase, A. Kaimai, K. Yashiro, Y. Nigara, J. Mizusaki, K. Kawamura, and H. Yugami, *Journal of The Electrochemical Society*, **149**(7), E252 (2002).
64. M. Kuhn, S. Hashimoto, K. Sato, K. Yashiro, and J. Mizusaki, *Journal of Solid State Chemistry*, **197**, 38 (2013).
65. T. Z. Ding, Y. M. Wang, and S. H. Shi, *Journal of Materials Science Letters*, **22**(1), 1 (2003).
66. J. H. Joo, R. Merkle, J.-H. Kim, and J. Maier, *Advanced Materials*, **24**(48), 6507 (2012).